Distributed cavity phase calculation for a rectangular Ramsey cavity in NRC-FCs1

Marmet, Louis; Dube, Pierre; Shtin, Nicolas; Lopez, J. Maricio

Publisher's version / Version de l'éditeur:
https://doi.org/10.1109/EFTF-IFC.2013.6702294
2013 Joint European Frequency and Time Forum & International Frequency Control Symposium (EFTF/IFC), pp. 764-767, 2013-07-25

Distributed cavity phase calculation for a rectangular Ramsey cavity in NRC-FCs1

Louis Marmet
Measurement Science and Standards
National Research Council
Ottawa, Ontario, Canada
Email: louis.marmet@nrc.ca

Nicolás Shtin
SMK Electronica S.A. de C.V.,
Aguila Azteca No. 19308,
Col. Baja Maq El Aguila,
22215 Tijuana, BC, México

Pierre Dubé
Measurement Science and Standards
National Research Council
Ottawa, Ontario, Canada

J. Mauricio López R.
Time and Frequency Division,
CENAM,
Queretaro, Qro. 76241, México

***Abstract*—A preliminary calculation of the frequency shifts resulting from the distributed phase of a rectangular cavity is used to model frequency measurements of the fountain clock NRC-FCs1. The calculation is based on a numerical evaluation of the cavity field made with a finite element EM solver. The frequency shift is obtained by solving the Bloch-equations numerically along the path of the atoms on the free-fall trajectories through the cavity. We study the frequency shifts as a function of the launch direction, the tilt of the physics package and offsets in the position of the MOT relative to the axis defined by the state-selection cavity and the Ramsey cavity.**

I. Introduction

The evaluation of frequency offsets arising in a Ramsey interrogation require a careful experimental evaluation of a fountain clock supported by numerical modeling of the electromagnetic field of the Ramsey cavity. The frequency of a fountain clock is dependent on phase variations in the rf-field and various geometrical factors. Phase variations arise from losses in the cavity walls and coupling to the antennas, all of which create traveling waves. The atomic motion through the phase variations produce first order Doppler shifts which are position dependent. As a result, distributed cavity phase (DCP) frequency shifts are often the leading contribution to the uncertainty of many fountain clocks [1]. Decades of work have resulted in a good understanding of DCP. However most atomic fountain clocks use TE_{011} cylindrical cavities while NRC-FCs1's design is based on a rectangular cavity and transversal C-field configuration borrowed from laboratory beam clocks. DCP calculations require three-dimensional solutions of the cavity field, a process which requires intensive computing resources. Simplifications to a two-dimensional problem exist for cylindrical cavities [2] but the symmetry of the system cannot be exploited advantageously for a rectangular cavity. However, decreasing costs of computer resources and improved performance of computers have reduced the time required to obtain results from a finite element model.

FCs1's Ramsey cavity is designed with conical below-cutoff waveguides in order to keep atoms away from the high fields near sharp edges and minimize phase shifts [3]. This configuration also gives a computational advantage since the atoms do not interact with the field where dense meshing calculations would be required. Our first partial numerical results show a behaviour consistent with the frequency shifts measured in NRC-FCs1 as a function of the launch direction, the tilt of the physics package and the choice of the antenna used to feed the Ramsey cavity. Measurements showed that a significant frequency difference exists between operation of the fountain clock with one antenna or the other. This difference may be a result of a misalignment of the MOT with respect to the axis defined by the state-selection and Ramsey cavities.

II. The physics package

The fountain clock NRC-FCs1 operates with a MOT loaded in $825\,\text{ms}$ and a launch cycle of $1575\,\text{ms}$ [4]. The atoms are trapped, accelerated and cooled with six $\sigma^+ - \sigma^-$ beams in the 110-configuration. They leave the MOT region in the $|F = 4, m_F\rangle$ states and are pumped to the $|F = 3, m_F = 0\rangle$ state by the state-selection cavity. The states remaining in the $|F = 4, m_F \neq 0\rangle$ are removed by a σ^+ polarized $4-5'$ pusher beam. Ramsey pulses are provided by a rectangular cavity

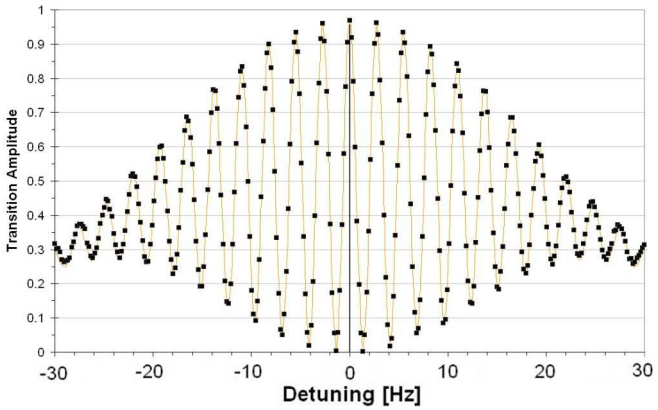

Fig. 1. Ramsey fringes for a 25cm fountain, one measurement per point.

operating in the TM_{210}-mode and fed with two magnetically-coupled antennas. A transversal C-field is generated by four linear electrodes. Because of a longer interaction between the atoms and the rf-field, the rectangular cavity produces a narrower Rabi pedestal than obtained with cylindrical cavities. In addition, it does not have field reversals in the neighborhood of the ends of the below-cutoff waveguides which could produce potentially large frequency shifts. Since the C-field is transversal the configuration takes advantage of a higher shielding from the inner cylindrical magnetic shield. The best short-term frequency stability is achieved at the optimal fountain height of 25 cm above the Ramsey cavity. The microwave signal is generated with a synthesizer chain synchronized with the NRC-SM1 maser which offered the best stability ($\sigma_y(\tau = 1s) < 2 \times 10^{-13}$). After Ramsey interrogation, the population in the $F = 4$ and $F = 3$ states is measured from the fluorescence signals obtained from four state-selecting beams: the $|F = 4\rangle$ detection beam, the pusher beam, the repumper beam, and another $|F = 4\rangle$ detection beam. Figure 1 shows the measured Ramsey fringes with a 96% contrast. An Allan deviation of $\sigma_y(\tau) = 3 \times 10^{-13}\,\tau^{-1/2}$ was obtained for $\tau < 10^5$ s. Changes to laser polarization in the detection system and the light shift contribute to the uncertainty by $< 10^{-15}$. The sample deviation of the frequency measurements show a repeatability $\sigma = 1.8 \times 10^{-15}$ over weeks of operation.

Six circular apertures can clip the atomic cloud during their free-flight. The lowest aperture, 162 mm above the MOT and 5.0 mm in diameter, is part of the lower light-shutter. The the cut-off waveguide of the state-selection cavity is located 186 mm above the MOT and has a diameter of 5.0 mm. A second light shutter has an aperture located 187 mm below the Ramsey cavity with a 10.5 mm diameter. The Ramsey cavity, located 768 mm above the MOT, has 10.5 mm diameter apertures at the ends of the cut-off waveguides each located 62 mm below and above the center of the cavity. The geometry of the system also includes detection beams having a 20 mm diameter. However, the intensity profile of these beams is not included in the current simulation.

III. Cavity field

The numerical evaluation of the field in the cavity is made using of a full-wave finite element EM solver (Ansoft HFSS finite element method solver). The precise shape of the cavity ($d_x = 39.2$ mm, $d_y = 26.67$ mm and $d_z = 18.0$ mm, and rounded internal corners) was reproduced in a CAD drawing in the solver. The dimension d_y was varied until the resonance frequency matched 9.192 GHz with $d_y = 26.84$ mm. The resonant frequencies of the model cavity are compared with the measured values in Table I. The RMS difference between theory and measurements for the remaining five modes is 45 MHz.

The Ramsey cavity is made of two identical copper halves held together symmetrically about the XZ-plane. The microwave signal is coupled into the cavity via two magnetic antennas (rectangular loops 2.6 mm $\times$0.5 mm) through 2.0 mm-wide slits located on the sides of the cavity (Fig. 2). The cutoff waveguides have cylindrical symmetry, with a conical shape near the cavity center in order to keep the atoms away from the high fields at the edges and minimize phase shifts. The cavity has a measured loaded $Q_{\text{measured}} = 4600$ and a numerically estimated unloaded $Q = 10000$.

TABLE I. Frequencies of the modes

Mode	Measured	Calculated
TM_{110}	7.036 GHz	6.999 GHz
TM_{210}	9.192 GHz	9.192* GHz
TE_{011}	9.262 GHz	9.280 GHz
TE_{111}	10.691 GHz	10.637 GHz
TM_{111}	11.019 GHz	10.967 GHz
TE_{211}	11.711 GHz	11.658 GHz

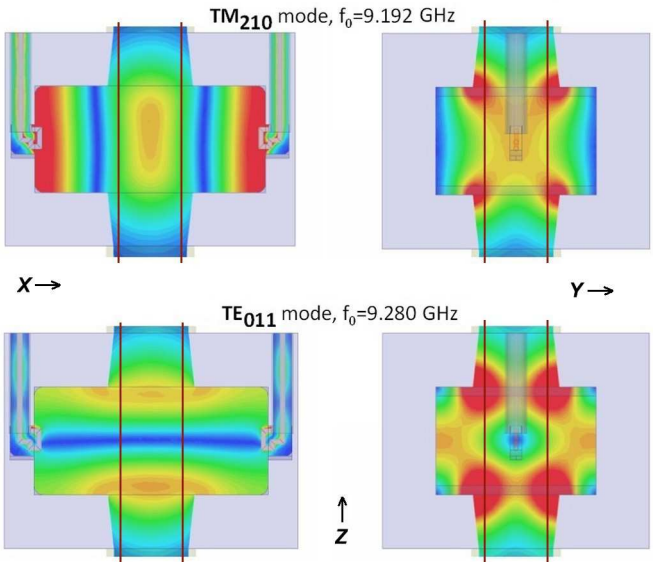

Fig. 2. Magnetic field amplitude for the TM_{210} and TE_{011} modes. The atoms are confined inside the space limited by the vertical lines.

The forward transmission plotted in Fig. 3 shows the resonances of the various modes. Two sharp dips occur at 9.2 GHz and 10.8 GHz. These are the result of destructive interference between three coupling fields (the two adjacent modes and the direct coupling from one antenna to the other) which occur when the first index l of the adjacent modes TM_{lmn} or TE_{lmn} have the same parity. The model gives a loaded $Q_{\text{model}} = 1000$. It is suspected that the exact position of the antennas is not modeled correctly which results in a larger coupling.

Although the finite element model includes in its solution every mode of the cavity, it is convenient to think of the field as the sum of many fields [1]. This could be useful to distinguish the small phase and amplitude variations generated by the solver from the errors generated by the calculations. Here we write the cavity field as the sum of a large amplitude standing wave $\mathbf{H}_0(\vec{r})$ representing the resonator's TM_{210} mode and other small amplitude fields representing an expansion of the non-resonant modes of the cavity and the field from the antennas:

$$\vec{H}(\vec{r}) = \vec{H}_0(\vec{r}) + \sum_k \left[\beta_k(\Delta\omega_k)\vec{h}_k(\vec{r})\right] + \vec{a}(\vec{r}),$$

where $\vec{H}_0(\vec{r})$ and $\vec{h}_k(\vec{r})$ are real and $\vec{a}(\vec{r})$ is the field from

the antennas. The fields $\vec{h}_k(\vec{r})$ are from other cavity modes and each factor $\beta_k(\Delta\omega_k)$ contains the phase and amplitude of the standing wave k relative to the phase and amplitude of the large standing wave at a detuning $\Delta\omega_k = \omega_{\mu\text{wave}} - \omega_k$. Using this expansion, it is possible to accurately evaluate the phase contributions of the non-resonant fields $\vec{h}_k(\vec{r})$ by calculating each one with the solver tuned on the resonant frequency of each mode k. The solutions for each field can be added differentially (with the factor $\beta_k(\Delta\omega_k)$) to the resonant solution for TM_{210} to study the effect on the phase.

IV. Frequency Shift

The frequency shift is calculated by simulating the path of the atoms along the free-fall trajectories through the cavity while solving numerically the Bloch equations using the differential form:

$$\begin{aligned} \delta u &= +\Delta\, v\, \delta t \\ \delta v &= -\Delta\, u\, \delta t + \Omega\, w\, \delta t \\ \delta w &= -\Omega\, v\, \delta t \end{aligned}$$

where $\Delta = 2\pi(f_{\text{mw}} - f_0)$, Ω is the Rabi frequency, f_{mw} is the frequency of the microwave field and f_0 is the atomic resonance frequency [5]. For this work, the Rabi frequency is derived from the Y component (parallel to the C-field) of the cavity field.

The calculation proceeds as follows. Initial positions and launch velocities of an atom are used to generate a set of trajectories $\vec{r}(t)$ through the physics package. Only trajectories which do not stop on any of the apertures are kept in the set. For each position along the trajectory intersecting regularly spaced constant-z planes inside the Ramsey cavity, $\vec{r}(nz_0)$, the field H and its phase Φ are sampled from the results of the finite element solver. A bilinear interpolation along the X- and Y- axes is made to obtain a list of field values $H(nz_0)$ and $\Phi(nz_0)$ at the locations $\vec{r}(nz_0)$. The lists are converted to time dependent values and smoothed using a spline fitting function. Starting with the Bloch vector $(u = 0, v = 0, w = -1)$, the Bloch equations are integrated along the trajectory with time intervals $\delta t = t(nz_0) - t((n-1)z_0)$.

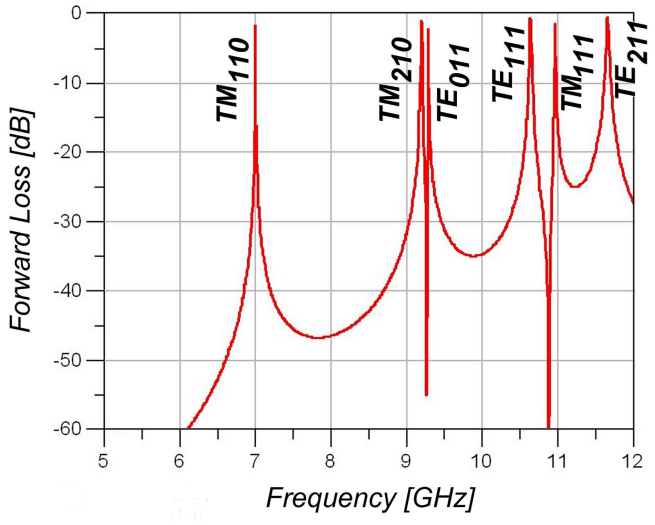

Fig. 3. Forward loss through Ramsey cavity. Canceling interference produces sharp dips between modes for which the parity of their first index is the same.

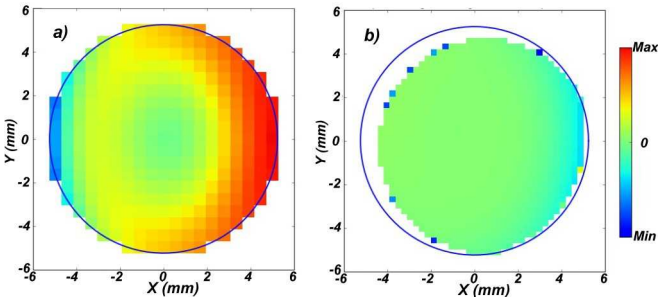

Fig. 4. Atomic population after Ramsey interrogation. The colour code represents the value w of the Bloch vector plotted as a function of the position of the atom at the exit of the Ramsey cavity. The antennas, located on the left- and right-hand side of the image, are labeled W and E respectively.

The initial launch velocities used for the calculation are selected according to a Gaussian velocity distribution representing the measured distributions along the three axes. Launching with a 110-configured MOT results in three different velocity distribution in the X-, Y- and Z-directions with equivalent temperatures $15.0\,\mu$K, $2.1\,\mu$K and $6.0\,\mu$K respectively [6]. For each trajectory a probability is assigned representing the probability of finding an atom within a velocity space element. A graph representing the population of the atoms (w component of the Bloch vector) as a function of the exit position after Ramsey interrogation is obtained from an average of the w values weighted by the probability of the trajectory. Two examples of the results are given in Fig. 4 for (a) two antennas and a tilted physics package and (b) one antenna and misaligned MOT. Atoms launched with a faster velocity are blocked at the edge of the apertures, resulting in a different excitation value seen as a dark pixel at the periphery of the disk. The frequency offset is found from the total population calculated at microwave frequencies $+f_m$ and $-f_m$ at half maximum on the Ramsey fringe.

V. Results and Discussion

The experimental conditions were reproduced numerically, with the physics package tilted ± 1 mrad from the vertical along the x and y directions. A perfect alignment of the MOT along the axis defined by the center of the state-selection and Ramsey cavities was used as well as as a MOT offset by $x = -1.8$ mm and $y = 0.9$ mm. In all cases, antenna-E, antenna-W (see caption of Fig. 4) and both antennas were tested. In order to simulate the use of the antenna-W, the field from antenna-E was used with the geometry rotated by $180°$ about the z-axis. The results are shown in Table II. The table shows the offsets normalized by $\sqrt{Q_{\text{model}}/Q_{\text{measured}}} = 0.47$ to compensate for the weaker antenna coupling of the measurement system.

The first block in the table lists results obtained with one antenna and a perfectly centered MOT. The relative frequency shift dy of the clock as a function of tilt varies by $dy/d\theta_x = 2.7 \times 10^{-15}$/mrad while $dy/d\theta_y < 0.1 \times 10^{-15}$/mrad. The effect does not change significantly when the MOT is misaligned ($x_0 = -1.8$ mm and $y_0 = 0.9$ mm), as shown in the second block of Table II. In this case, the frequency shift as a function of tilt is $dy/d\theta_x = 2.1 \times 10^{-15}$/mrad

TABLE II. CALCULATED FREQUENCY SHIFTS

Number of Antennas	Initial position x_0, y_0[mm]	v_x, v_y [mm/s]	Tilt θ_X, θ_Y [mrad]	Frequency Offset $\left[10^{-15}\right]$
1	0, 0	0, 0	0, 0	-5.0
1	0, 0	0, 0	-1, 0	-8.0
1	0, 0	0, 0	$+1$, 0	-2.7
1	0, 0	0, 0	0, -1	-5.1
1	0, 0	0, 0	0, $+1$	-5.1
1	$-1.8, +0.9$	$+16, -8$	$-4, +2$	-5.6
1	$-1.8, +0.9$	$+16, -8$	$-5, +2$	-7.7
1	$-1.8, +0.9$	$+16, -8$	$-4, +1$	-5.8
1	$+1.8, -0.9$	$-16, +8$	$+4, -2$	-1.8
1	$+1.8, -0.9$	$-16, +8$	$+5, -2$	$+1.7$
1	$+1.8, -0.9$	$-16, +8$	$+4, -1$	-2.3
2	0, 0	0, 0	0, 0	-4.9
2	0, 0	0, 0	± 1, 0	-5.2
2	0, 0	0, 0	0, ± 1	-5.0
2	$\mp 1.8, \pm 0.9$	$\pm 16, \mp 8$	$\mp 4, \pm 2$	-3.6
2	$-1.8, +0.9$	$+16, -8$	$-5, +2$	-3.0
2	$-1.8, +0.9$	$+16, -8$	$-4, +1$	-4.0

and $dy/d\theta_y = 0.2 \times 10^{-15}$/mrad. However, the misaligned MOT produces an asymmetry in the system and the frequency difference $\Delta f = 3.8 \times 10^{-15}$ arises when the other antenna is used. In the last case, when both antennas are used, the frequency offset has a weak dependence on tilt remaining $dy/d\theta < 0.2 \times 10^{-15}$/mrad for small angles (third block in Table II. However a constant offset is present due to a quadratic dependence of the DCP not canceled by the two antennas. A change in the launch direction does not cause a significant effect, mostly as a result of the velocity selection made by the apertures of the Ramsey cavity.

The measured frequency shifts as a function of tilt are: for antenna-E $dy/d\theta_x = 1 \times 10^{-15}$/mrad and $dy/d\theta_y = 5 \times 10^{-15}$/mrad; for antenna-W $dy/d\theta_x = 3 \times 10^{-15}$/mrad and $dy/d\theta_y = 3 \times 10^{-15}$/mrad. All measurements have an uncertainty of 1.8×10^{-15}/mrad. The measured frequency are comparable to the calculated values. However, the measured frequency shift between the two antennas is 18×10^{-15} which seems to indicate that the misalignment of the MOT is even greater than the numbers used in the model. This could also explain some of the variations in the measured $dy/d\theta$.

It is possible that the position of the MOT is shifted away from the symmetry axis due to the asymmetric construction of the electrostatic shutters [4]. The shutter enclosures are 20 cm diameter disks installed off-axis. When under vacuum, the compressed disks may flex in a way to produce a misalignment. Correction coils were added for the added possibility of centering the MOT (X and Y directions) and shift the launch location. The model helps in determining the direction the MOT has to be moved to correct the offset.

VI. CONCLUSIONS

The numerical method presented in this work produces consistent evaluations of the DCP frequency shifts in a rectangular Ramsey cavity and are consistent with the measured results obtained with NRC-FCs1. The model brings a better understanding of the causes of the frequency shifts. Two principal contributions arise from a misalignment of the MOT and a strong coupling of the antennas resulting in an important flux from antenna to the other.

Further work is required to complete this evaluation. A model with the correct $Q_{\text{loaded}} = 4600$ is necessary and the field of the state-selection cavity can be added to the simulation. Contributions from phase gradients of other modes should be calculated separately and added as a perturbation to the field. This would provide a good check of the results of the finite element solver. The coupling of the antennas can also be separated from the unloaded cavity modes by using the eigenmode solver. One can thus verify that the frequency offsets are mainly due to the coupling between the antennas. Finally, the intensity distribution of the laser beams can be accounted for, but this is not expected to change the results significantly.

ACKNOWLEDGMENT

L.M. would like to thank Ph. Laurent (Observatoire de Paris) and K. Szymaniec (NPL) for useful discussions and advice on the distributed cavity phase shift. The computations were made in the Python computing language with the Numpy, Scipy and Matplotlib extensions and IPython interactive computing [7].

REFERENCES

[1] R. Li, K. Gibble, "Evaluating and minimizing distributed cavity phase errors in atomic clocks," Metrologia 47, 534, 2010, and references therein

[2] R. Li, K. Gibble, "Phase variations in microwave cavities for atomic clocks," Metrologia 41, 376, 2004

[3] C. Fertig, R. Li, J.I. Rees, K. Gibble, "Distributed Cavity Phase Shifts & Microwave Photon Recoils," Proceedings of the 2002 IEEE International Frequency Control Symposium and PDA Exhibition, 469, 2002

[4] L. Marmet B. Hoger, P. Dubé, A.A. Madej, J.E. Bernard, "Detailed description of FCs1: NRCs cesium fountain primary standard," Proceedings of the 2008 IEEE International Frequency Control Symposium, 386, 2008

[5] L. Allen and J.H. Eberly, "Optical Resonance and Two-Level Atoms," Dover Publications, Inc., New York, N.Y. (1987)

[6] L. Marmet, "Update on the development of NRC-FCs1," Proceedings of the IEEE International Frequency Control Symposium Joint with the 22nd European Frequency and Time forum, Besan con France, 562, 2009

[7] F. Pérez and B.E. Granger, "IPython: a System for Interactive Scientific Computing," Comput. Sci. Eng., Vol. 9, No. 3, pp. 21–29, May 2007